International Journal of Biological Macromolecules 223 (2022) 1145–1157

Contents lists available at ScienceDirect

International Journal of Biological Macromolecules

journal homepage: www.elsevier.com/locate/ijbiomac

# Molecular mechanism of ion channel protein TMEM16A regulated by natural product of narirutin for lung cancer adjuvant treatment

Sai Shi [a,b,1], Xue Bai [a,1], Qiushuang Ji [c,1], Haifu Wan [a], Hailong An [d], Xianjiang Kang [a], Shuai Guo [a,*]

[a] School of Life Sciences, Hebei University, Baoding 071002, Hebei, China
[b] Tianjin Key Laboratory of Function and Application of Biological Macromolecular Structures, School of Life Sciences, Tianjin University, Tianjin 300072, China
[c] School of Pharmaceutical Science and Technology, Tianjin University, Tianjin 300072, China
[d] School of Health Sciences and Biomedical Engineering, Hebei University of Technology, Tianjin 300401, China

ARTICLE INFO

*Keywords:*
TMEM16A ion channel protein
Narirutin
Molecular mechanism
Synergistic anticancer
Adjuvant therapy

ABSTRACT

Cancer chemotherapy drugs are widely criticized for their serious side effects and low cure rate. Therefore, adjuvant therapy as a combination with chemotherapy administration is being accepted by many patients. However, unclear drug targets and mechanisms limit the application of adjuvant treatment. In this study, we confirmed TMEM16A is a key drug target for lung adenocarcinoma, and narirutin is an effective anti-lung adenocarcinoma natural product. Virtual screening and fluorescence experiments confirmed that narirutin inhibits the molecular target TMEM16A, which is specific high-expression in lung adenocarcinoma. Molecular dynamics simulations and electrophysiological experiments revealed the precise molecular mechanism of narirutin regulating TMEM16A. The anticancer effect of narirutin and its synergistic effect on cisplatin were explored by cell proliferation, migration, and apoptosis assays. The signaling pathways regulated by narirutin were analyzed by western blot. Tumor xenograft mice experiments demonstrated the synergistic anticancer effect of narirutin and cisplatin, and the side effects of high concentrations of cisplatin were almost eliminated. Pharmacokinetic experiments showed the biological safety of narirutin is satisfactory *in vivo*. Based on the significant anticancer effect and high biosafety, naringin has great potential as a functional food in the adjuvant treatment of lung cancer.

## 1. Introduction

Cancer is a malignant disease with high mortality rate in humans, and its incidence has increased in recent years [1,2]. Lung cancer ranks first as the cause of morbidity and mortality among all cancer types [3]. The incidence of lung cancer is increasing in the younger population and in women, making it an increasingly serious threat to human health [4]. Lung adenocarcinoma is a major subtype of lung cancer, accounting for 40–55 % of cases [5]. Lung adenocarcinoma originates in the bronchial epithelium and mucous glands. It is asymptomatic in the early stages and lacks specificity in the late stages; therefore, it is often misdiagnosed, and the optimal treatment period is missed [6,7]. Presently, patients with lung adenocarcinoma are mainly treated with individualized treatment plans that integrate multidisciplinary options, including chemotherapy, radiotherapy, surgery, and other adjuvant treatments [8–10].

Chemotherapeutic drugs for lung cancer treatment include broad-spectrum anticancer drugs, such as cisplatin (DDP), doxorubicin, and paclitaxel, but the side effects of many of them are severe [11–13]. Long-term use of DDP causes nephrotoxicity, bone marrow suppression, and liver damage and is accompanied by gastrointestinal adverse reactions, such as nausea, vomiting, and diarrhea [14–16]. These side effects cause both physical and psychological harm to patients, so that many cancer patients experience complications such as depression and anxiety during treatment [17,18]. Therefore, adjuvant drugs for lung adenocarcinoma to reduce side effects and improve drug efficacy through low-dose multi-target combined administration are being explored for individualized tumor therapy. Food adjuvant therapy is favored by cancer patients because of its safety, pain-free, low cost, and operational ease [19,20].

Functional foods help prevent and treat cancer. Approximately 35 %

* Corresponding author.
*E-mail address:* guoshuai@hbu.edu.cn (S. Guo).
[1] These authors contributed equally to this work.

https://doi.org/10.1016/j.ijbiomac.2022.11.123
Received 19 September 2022; Received in revised form 10 November 2022; Accepted 12 November 2022
Available online 15 November 2022

of human cancers are closely related to dietary factors [21,22]. The incidence of breast, gastric, and colon cancers can be reduced by diversifying food intake, limiting sugar intake, and reducing dietary animal fat content [23–25]. Additionally, functional foods inhibit cancer growth through multiple pathways. For example, lycopene inhibits the production of oxidative free radicals through anti-oxidation, which delays cancer growth [26]. Astaxanthin significantly inhibits oral cancer by inducing cell cycle arrest, lysosomal acidification, and apoptosis [27]. Although various functional foods have been shown to have anticancer effects, most of their targets and mechanisms are unclear, which greatly limits their use as anticancer functional foods [28,29].

Drug screening based on specific protein targets is a classic drug development strategy to explore anti-lung adenocarcinoma functional foods. TMEM16A is endogenously highly expressed in lung cancer tissues [30,31]. It modulates the osmotic pressure of cancer cells by regulating intracellular and extracellular $Cl^-$ concentrations to change the cell shape. Cell morphology changes directly impact cancer cell proliferation, migration, and invasion [32,33]. In addition, TMEM16A also forms an interaction network with EGFR proteins and ezrin–radixin–moesin (ERM) proteins, and it regulates the growth of cancer cells through signal transduction [34,35]. TMEM16A is only expressed in specific normal tissues but is abnormally upregulated in cancer cells, so it is a suitable drug target for lung adenocarcinoma treatment [36].

In this work, virtual screening found that the binding affinity of natural product narirutin and TMEM16A protein was high. Subsequently, fluorescence and electrophysiological experiments verified that narirutin was an effective TMEM16A inhibitor. Molecular modeling, cell experiments and animal experiments confirmed the anticancer effect and mechanism of narirutin *in vitro* and *in vivo*. The combination of low-concentration narirutin and DDP achieved synergistic anticancer effects and reduced the side effects of DDP. Therefore, narirutin is a potential functional food for adjuvant therapy of lung adenocarcinoma.

## 2. Materials and methods

### 2.1. Virtual screening

To screen for safe and reliable TMEM16A inhibitors, the molecular docking software Vina [37] was used to perform virtual screening of a compound library containing >5000 natural products (provided by Chengdu DeSiTe Biological Technology Co., Ltd. of China, http://www.028desite.com/). The calcium-bound structure of TMEM16A (PDB ID: 5OYB) was programmed to be docking receptor. The extracellular vestibule of the TMEM16A channel as the inhibitor binding pocket was set to docking box. The PDBQT files of TMEM16A and ligands were prepared by Autodock [38], TMEM16A was set to rigid, and the ligand was flexible. The grid center was determined according to the center of the binding pocket, and the searching space size was 24 $Å^3$. The global search exhaustiveness value was set to 50. The maximum energy difference between the optimal binding mode and the worst case was set to 5 kcal/mol to ensure diverse docked poses.

### 2.2. YFP fluorescence quenching assay

LA795 cells were cultured in a standard cell incubator with RPMI1640 medium. YFP-F46L/H148Q/I152L plasmid was transfected to LA795 cells, and the fluorescence was excited with 488 nm and detected at 520 ± 15 nm. When TMEM16A ion channels in the membrane were activated, $I^-$ in the bath solution entered cells through the channels to quench YFP fluorescence. However, the channels could not be activated by $E_{act}$ (a TMEM16A activator; CAS: 461000-66-8, MCE, New Jersey, USA) [39] if the cells were incubated with TMEM16A inhibitor so that the YFP fluorescence was kept bright. The blank control group has not contained any drug. The $E_{act}$ group was added with 20 μM $E_{act}$ at the time marked by arrow, the $T16A_{inh}$-A01 (a TMEM16A inhibitor; CAS: 552309-42-9, MCE, New Jersey, USA) [40] group and the Narirutin (CAS: 14259-46-2, Solarbio, Beijing, China) group contained 20 μM $T16A_{inh}$-A01 or 100 μM narirutin in the bath solution, and 20 μM $E_{act}$ was added at the arrow mark on this basis. The bath solution was PBS buffer containing 150 μM NaI. Fluorescence was detected by a confocal laser scanning microscope (IX83-FV3000, Olympus, Tokyo, Japan).

### 2.3. Electrophysiology

Electrophysiology data was recorded by HEKA patch clamp (HEKA Elektronik, Lambrecht, Germany). Patch pipettes were pulled to resistance of 3–5 MΩ using a P97 puller (Sutter Instrument, Novato, USA). Data were low pass filtered at 2.9 kHz, sampled at 10 kHz, and recorded by Pulse software with a Digi LIH1600 interface (HEKA, Lambrecht, Germany). The stimulation voltage waveform was a step voltage from −80 to +80 mV. Solutions were prepared as described previously [41]. Bath solution: 150 mM NaCl, 1 mM $MgCl_2{\cdot}6H_2O$, 10 mM HEPES, 10 mM glucose, and 10 mM mannitol; the solution was adjusted to pH 7.4 using NaOH. Pipette solution: 130 mM CsCl, 10 mM EGTA, 1 mM Mg-ATP, 1 mM $MgCl_2{\cdot}6H_2O$, and 10 mM HEPES; the solution was adjusted to pH 7.4 using CsOH. The 600 nM $Ca^{2+}$ in the pipette solution was calculated using CaEGTA Calculator V1.2: https://somapp.ucdmc.ucdavis.edu/pharmacology/bers/maxchelator/CaEGTA-NIST.htm.

### 2.4. Molecular dynamics simulations

CHARMM-GUI [42] was used to construct the TMEM16A simulation system. TMEM16A protein was inserted into POPC lipid bilayers, and a solvated system was added with 150 mM KCl. Simulations were performed using Amber16 [43] of Amber ff14SB force field, lipid14 force field, and Joung/Cheatham ion parameters [44,45]. Parametrization of narirutin was performed using the Antechamber module of Amber16.

Before the production simulation, the system of solutions, membranes, and the entire system were sequentially performed for energy minimization. The system temperature was increased from 0 to 100 K and 100 to 300 K under the NVT and NPT ensemble, respectively, and the protein was restrained (10 $kcal{\cdot}mol^{-1}{\cdot}Å^{-2}$). An NPT equilibration of 300 ps was performed. The water molecules were filled the pore, protein Cα atoms were restrained with a constraint force of 2 $kcal{\cdot}mol^{-1}{\cdot}Å^{-2}$. Two independent 100 ns simulations were performed under NPT conditions at 300 K and 1 bar in the simulation. With two independent subunits in each system, quadruple sampling can finally be achieved. The final simulations used Langevin thermostat and Monte Carlo constant pressure device with a non-viscous cutoff of 10 Å. Long-range electrostatic interactions and van der Waals interactions were cut off at 12 Å. The MD time step was set to 2 fs. The generated trajectories were analyzed by The CPPTRAJ module of the Amber program. Visualization and analysis of model features were performed by VMD 1.9.2 program [46] and Open-Source Pymol (https://pymol.org).

### 2.5. Quantum chemical calculation

The electrostatic surface potential analysis of drugs and residues was calculated by density functional theory. The molecular wave function information was calculated by Gaussian 03 as described previously [47]. Wave function data were generated using the B3LYP/6-31G** level algorithm and molecular surface analysis maps were visualized by Multiwfn [48] and VMD 1.9.2 program [46].

### 2.6. Site-directed mutagenesis

Mutagenesis primers were designed by Agilent Primer Design Website (https://www.agilent.com.cn/store/primerDesignProgram.jsp): T385A Primer, 5′-cctctgtgtgacaaggcctgcagctactgga-3′. N525A Primer, 5′-cagccttggccatggcctcctccccgtctg-3′. R535A Primer, 5′-

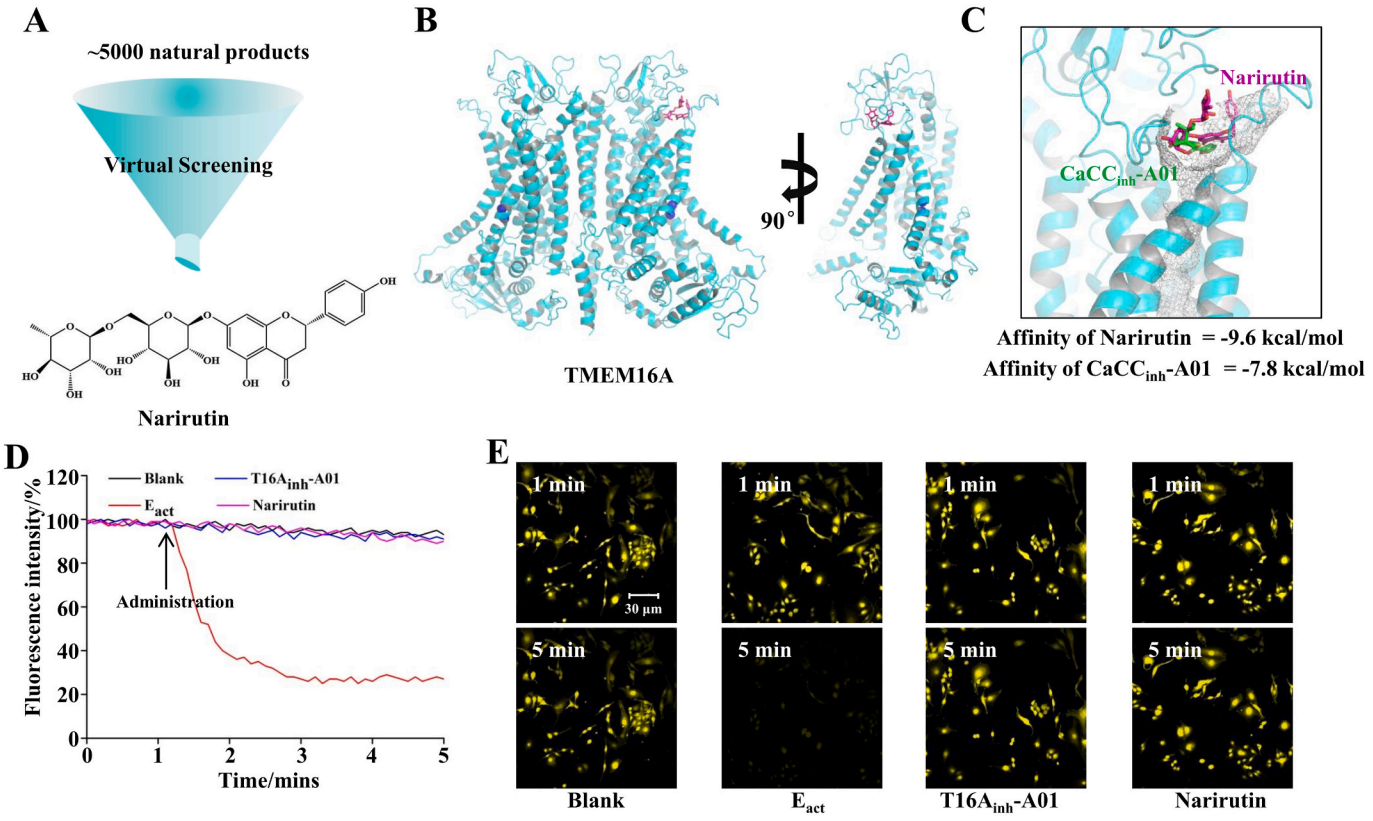


**Fig. 1.** Narirutin is an ingredient TMEM16A inhibitor. (A). Virtual Screening flowchart. (B). TMEM16A inhibitor binding pocket. (C). Binding conformation of narirutin and CaCC$_{inh}$-A01 to TMEM16A. (D). YFP fluorescence quenching curves of blank control, E$_{act}$, T16A$_{inh}$-A01 and narirutin in LA795 cells. (E). Real-time YFP fluorescence images at 1 and 5 min ($n$ = 3).

gtgcggtccaacatcgcggttacagtcacggc-3′. R621A Primer, 5′-catcttccgctctttcgcgatggaggagtgtgcc-3′. E623A Primer, 5′-tctttccggatggcggagtgtgccccg-3′. E624A Primer, 5′-ccggatg-gaggcgtgtgccccgg-3′.

### 2.7. CCK-8 and Colony formation assay

Cells were cultured in 96-well plates and incubated with drugs for 24 h. Then, 10 μL CCK-8 (Solarbio, Beijing, China) was added to each well for 2 h. The absorbance at 450 nm was detected, and the cell viability was defined as the absorbance of the test group divided by that of the control group.

Cells were cultured in 6-well plates with 100 cells in each well and incubated with drugs for 2 weeks. The cells were washed with PBS and stained with Giemsa. The number of colonies was statistically analyzed by ImageJ software (National Institutes of Health, Bethesda, USA).

### 2.8. Wound healing assay

Cells were c scraped with a 10 μL tip and cultured with low nutrient medium containing drugs. Cells were photographed at 0, 24, 48, and 72 h using a Nikon microscope (TE2000-S, Tokyo, Japan). The relative wound area was calculated by dividing the experimental group by the control group analyzed by ImageJ software.

### 2.9. Annexin-V assay

Cells were cultured with drugs for 24 h and collected. Cells were incubated with binding buffer containing annexin V-FITC and propidium iodide (PI) (Solarbio, Beijing, China). Samples were analyzed by CytoFLEX flow cytometer (Beckman Coulter, California, USA).

### 2.10. Western blot

Cells were cultured with drugs for 24 h in 6-well plates and collected. Cells ($10^6$) were lysed by RIPA cell lysate, and 20 μg proteins were added to each well. The proteins were separated on 8 % sodium dodecyl sulfate-polyacrylamide gels and electroblotted onto PVDF membrane at 80 V. The blots were incubated overnight with antibodies and incubated with corresponding secondary antibodies. Blots were detected by Chemiluminescence imaging system (BIO-RAD, California, USA).

### 2.11. Tumor xenografts in mice

All the animal experiments were approved by the Animal Welfare and Ethical Committee of Hebei University Experimental Animal Center. The approval number for this work is IACUC-2021XG033. LA795 cells were inoculated to Balb/c mice (6- to 8-week-old) in the right forelimb. Tumor volumes were measured every 5 days and calculated with the formula of length × width$^2$ / 2. The mice were divided into 6 groups when the tumor volume reached 150 mm$^3$: (1) control group, (2) 30 μM narirutin (17.43 mg/kg) group, (3) 60 μM narirutin (34.86 mg/kg) group, (4) 10 μM DDP (3 mg/kg) group, (5) 20 μM DDP (6 mg/kg) group, and (6) 30 μM narirutin + 10 μM DDP group. Drugs were administrated to mice *via* intragastric administration. Mice were injected 6 times and measured 7 times. All the mice were sacrificed after 7 times measurements.

### 2.12. Pharmacokinetic study of narirutin in mice

100 μM (58.1 mg/kg) of narirutin were intragastric administration to rats. 200 μL of blood was collected from the orbit at different times. Agilent 1100 high performance liquid chromatograph (Agilent

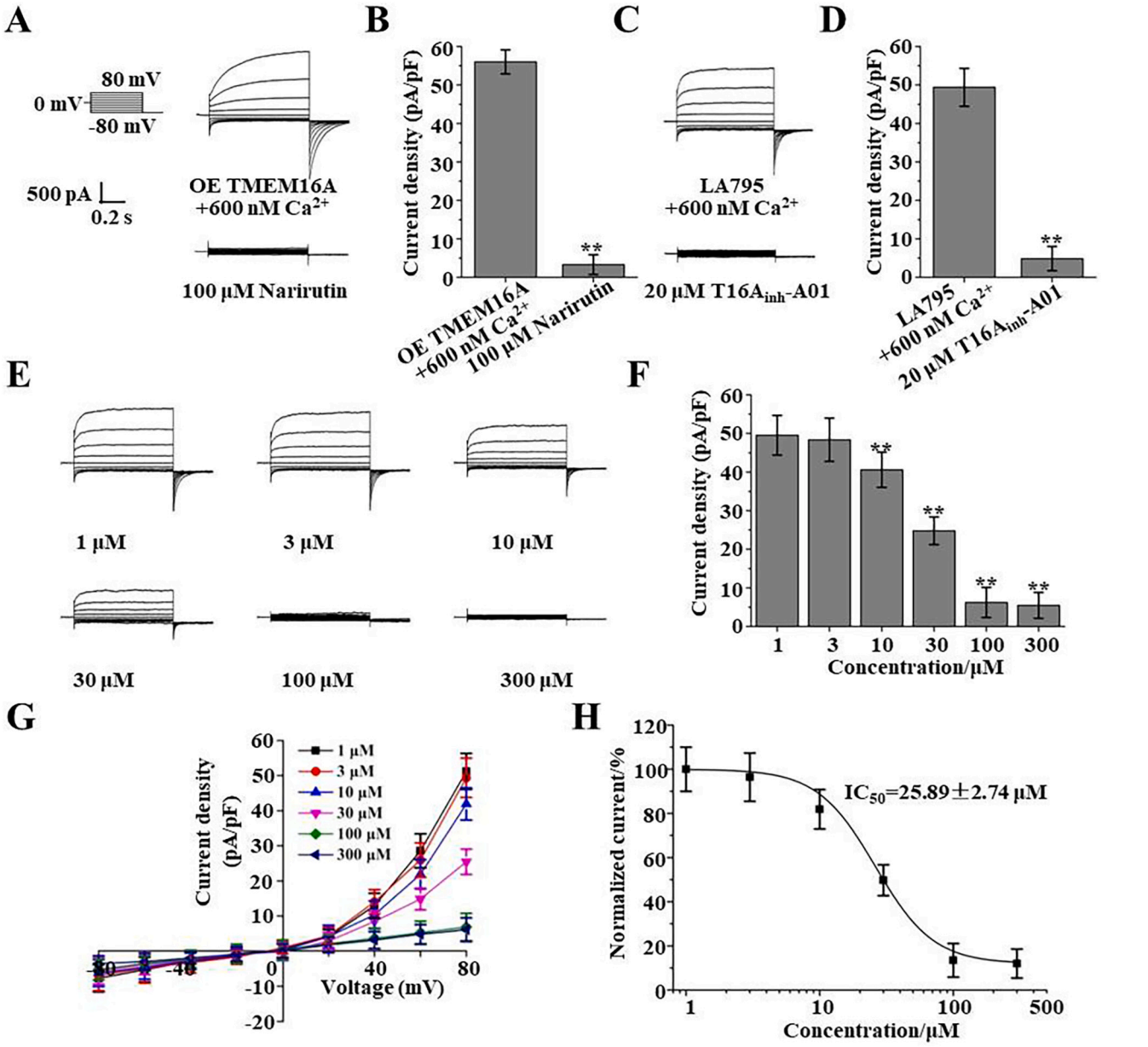


**Fig. 2.** Narirutin inhibited TMEM16A whole-cell current in LA795 cells. (A). Typical TMEM16A whole-cell currents of HEK293 cells transfected with TMEM16A and the currents were inhibited by 100 μM narirutin ($n = 5$). (B). Statistical results of (A). (C). Typical TMEM16A whole-cell currents in LA795 cells inhibited by $16A_{inh}$-A01 ($n = 5$). (D). Statistical results of (C). (E). Typical TMEM16A whole cell currents inhibited by different concentrations of narirutin ($n = 5$). (F). TMEM16A currents at +80 mV with varying concentrations of narirutin ($n = 5$). (G). The current density-voltage curve of TMEM16A inhibited with different concentrations of narirutin ($n = 5$). (H). Dose-response curve for narirutin inhibition of TMEM16A currents in LA795 cells ($n = 5$).

Technology Co., Ltd., USA) with Agilent Zorbax-SB C18 column (4.6 mm × 150 mm, 5 μm) was used for chromatographic analysis. The mobile phase was acetonitrile water (20:80). The flow rate was 1.0 mL/min, and the detection wavelength was 283 nm. The pharmacokinetic parameters were fitted by DAS 2.0 software.

### 2.13. Data analysis

Origin 9.0 was used for graphic creation and statistical data analysis. All data were presented as mean values ± SD. Independent-samples *t*-test or paired-samples *t*-test was used for statistical evaluations of different group comparisons. Asterisks indicate significant differences ($^*P < 0.05$, $^{**}P < 0.01$).

## 3. Results

### 3.1. Food ingredient narirutin is a natural TMEM16A inhibitor

Virtual screening based on the target protein binding pocket is an effective method for drug development. Virtual screening of 5000 natural product molecules was performed using open-source docking technology with TMEM16A. The drug binding pocket of TMEM16A confirmed previously was set as the receptor docking region for molecular docking [49]. The results showed that the food ingredient narirutin formed a stable binding conformation with TMEM6A (Fig. 1A). The conformation of narirutin binding to TMEM16A is shown in Fig. 1B. Local magnified results showed that narirutin bind to the extracellular vestibule region of the pore of TMEM16A which was similar to $CaCC_{inh}$-A01, and the affinity of narirutin was higher than $CaCC_{inh}$-A01 (Fig. 1C).

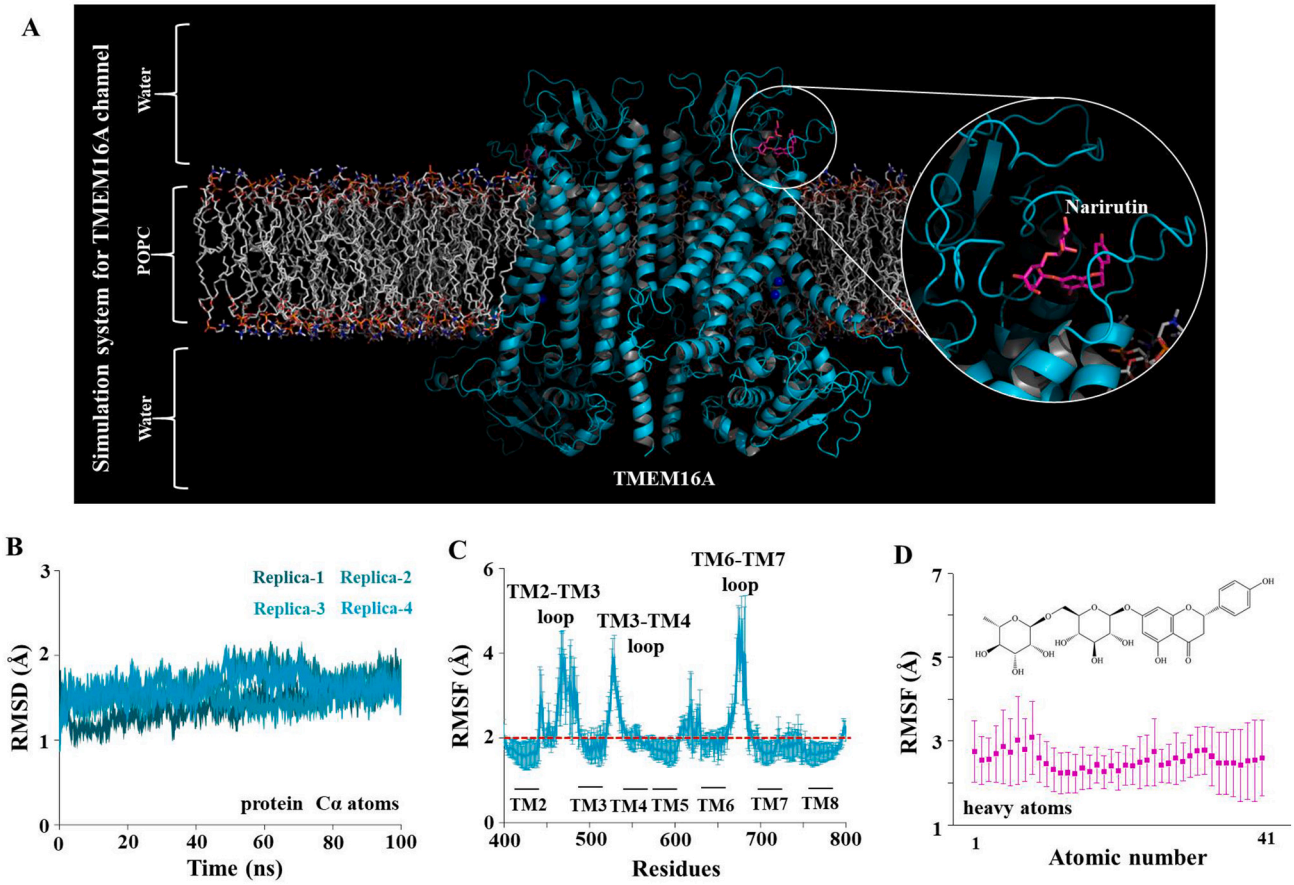


**Fig. 3.** Molecular dynamics simulation of the TMEM16A system. (A). Simulation of the TMEM16A system. TMEM16A was shown in cartoon; POPC was shown in stick (gray). Narirutin was shown as magenta sticks. (B). The root means square deviation (RMSD) of the TMEM16A protein. (C). The root means square fluctuation (RMSF) of the TMEM16A protein. (D). The RMSF of heavy atoms of narirutin.

YPF fluorescence quenching assays were performed to verify the inhibitory effect of narirutin on TMEM16A. The results showed that activation of TMEM16A by 10 μM $E_{act}$ led to quenching of cellular YFP fluorescence, whereas $T16A_{inh}$-A01 and narirutin inhibited the activation of $E_{act}$ (Fig. 1D). Real-time fluorescence images (at 1 and 5 min) showed that narirutin achieved the same inhibitory effect as the TMEM16A inhibitor, $T16A_{inh}$-A01 (Fig. 1E). Combined virtual screening and fluorescence results demonstrate that the food ingredient narirutin is a potent TMEM16A inhibitor.

### 3.2. Narirutin concentration dependently inhibits TMEM16A whole-cell currents

Whole-cell patch clamp experiments were performed to evaluate the inhibitory effect of narirutin on TMEM16A. First, exogenous transfection of TMEM16A in HEK293 cells showed that 100 μM narirutin inhibited the TMEM16A whole-cell current by >90 % (Fig. 2A and B). The $Cl^-$ current in LA795 cells was detected using the same experimental system, and the current was inhibited by $T16A_{inh}$-A01 (Fig. 2C and D). Different concentrations of narirutin were then added to the bath solution, and the changes in TMEM16A currents were recorded (Fig. 2E). Statistical results indicated that TMEM16A was almost completely inhibited by narirutin above 100 μM (Fig. 2F). The current density-voltage curve showed that narirutin mainly inhibited the outward current of TMEM16A (Fig. 2G). The Hill equation was used to fit the inhibitory effect of different concentrations of narirutin, and its $IC_{50}$ was 25.89 ± 2.74 μM (Fig. 2H). Thus, narirutin inhibited endogenous TMEM16A currents in a concentration-dependent manner in LA795 cells.

### 3.3. Dynamic behavior of narirutin binding to TMEM16A

To investigate the stability of TMEM16A binding to narirutin, a complex simulation system was constructed, including TMEM16A, narirutin, water, ions, and POPC (Fig. 3A). The docking conformations of narirutin were placed in chains A and B of TMEM16A. The root mean square deviation (RMSD) of TMEM16A was calculated to evaluate the conformational stability of the complex system during MD simulations. As shown in Fig. 3B, RMSD values of the protein backbone atoms ranged between 1.56 and 1.74 Å relative to the initial structure. The mobility of the protein residues was examined by plotting the root-mean-square fluctuation (RMSF) of the backbone atoms of the TMEM16A residue. RMSF values of all the helices in the pore region were <2 Å (Fig. 3C), which indicated that the proteins in the system were stable. The average RMSF of the narirutin heavy atoms in the quadruplet trajectories is <3 Å (Fig. 3D), indicating that it is stable in this binding mode.

### 3.4. Binding mode of narirutin and TMEM16A

To reveal the mode of interaction of narirutin with TMEM16A, the free energy landscape of narirutin bound to TMEM16A was mapped. RMSD and radius of gyration of narirutin were calculated. These data were used as reaction coordinates to determine the lowest-energy conformation of narirutin (Fig. 4A). The results showed the presence of a stable bound state of narirutin in binding mode (Fig. 4A). As shown in Fig. 4B, narirutin formed six interactions with the 22 residues in the binding pocket. Among them, H-bond interactions with A523, T385, R621, E623, E624, and N525; C-carbon H-bond with D383, C386, R535, and E623; alkyl interactions with R531 and K384; π-cation interactions

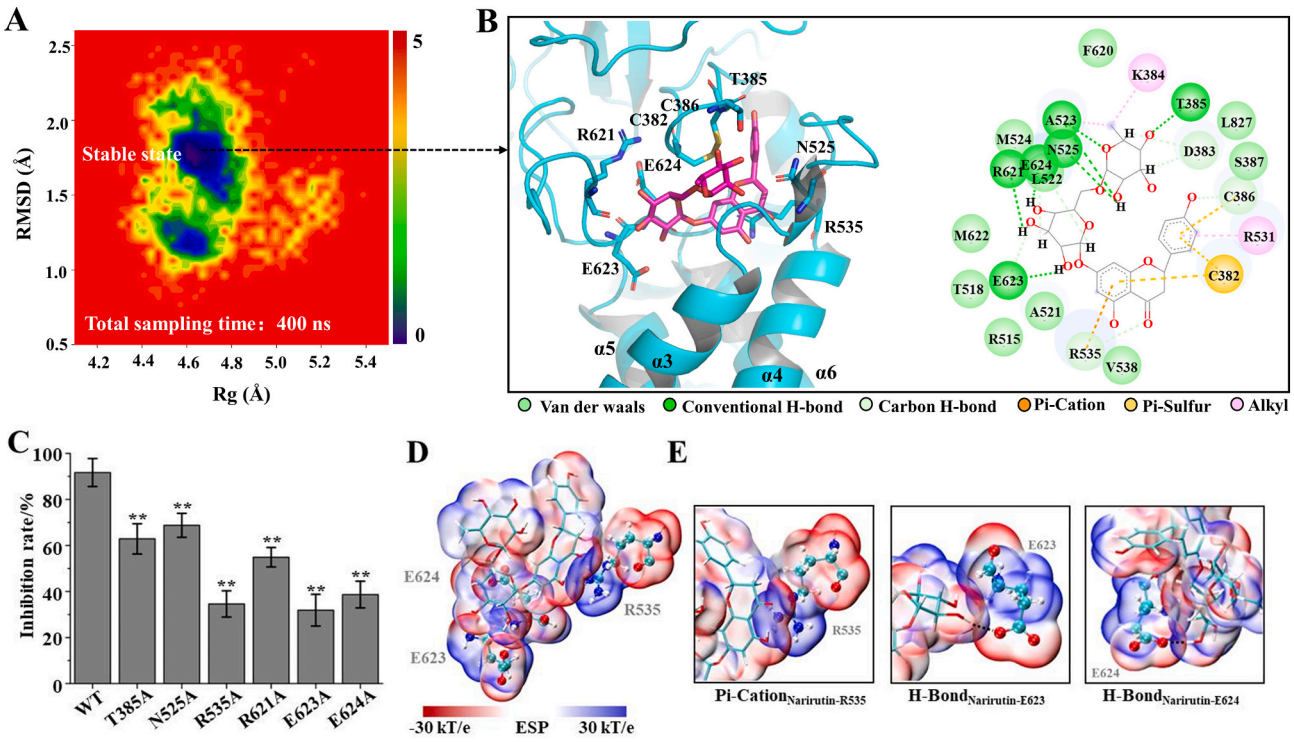


**Fig. 4.** Binding mode of narirutin and TMEM16A. (A). Free energy landscape of the narirutin binding mode. (B). Representations of the binding mode of the narirutin and TMEM16A in the lowest binding energy conformation. (C). Inhibition rate of different TMEM16A mutants by 100 μM narirutin ($n$ = 3). (D). ESP-mapped molecular VDW surface of narirutin and R535/E623/E624. (E). Pi-Cation and H-bond interaction between Narirutin and R535/E623/E624.

with R535; π-sulfur interactions with C386 and C382; and van der Waals interactions with V538, A521, R515, T518, M622, M524, F620 L827, and S387 (Fig. 4B). These interactions allowed narirutin to bind stably above the pores of the TMEM16A channel, thus blocking the pores.

Molecular mutagenesis was performed to verify the mode of binding of narirutin to the TMEM16A channel. Six residues (T385, N525, R535, R621, E623, and E624) that interacted electrostatically with narirutin were mutated to alanine. The inhibition of mutants by 100 μM narirutin showed that the above sites significantly affected the inhibition of the TMEM16A channel by narirutin, especially R535, E623, and E624. The electrostatic surface potentials of narirutin with R535, E623, and E624 in the steadiest state were calculated to characterize the electrostatic interactions. As shown in Fig. 4D and E, there was an overlap of van der Waals surfaces at the three sites where R535/E623/E624 bound with narirutin, and the electrical properties of the overlapping regions were complementary. This result indicates that the benzene ring in the structure and the hydroxyl group on the sugar ring are crucial for the binding of narirutin and TMEM16A.

### 3.5. Narirutin mediated regulation of TMEM16A potentiates the inhibitory effect of DDP on lung adenocarcinoma cell proliferation

TMEM16A expression is positively correlated with cancer cell proliferation. Therefore, the regulatory effect of narirutin-mediated inhibition of TMEM16A on the proliferation of LA795 cells was tested using CCK-8 and colony formation assays. CCK-8 results indicated that narirutin inhibited LA795 cell viability in a concentration-dependent manner (Fig. 5A). Next, TMEM16A in LA795 cells was knocked down using shRNA to confirm that TMEM16A was the target of narirutin. The viability of LA795 cells was significantly reduced after transfection with shRNA, and adding 30 μM narirutin on this basis did not further reduce cell viability, which proved that TMEM16A was the target of narirutin. Because DDP mainly acts on different targets along with narirutin, we evaluated the combined administration of DDP and narirutin. Co-administration of 10 μM DDP and 30 μM narirutin produced additive effects on cell viability inhibition, and TMEM16A shRNA combined with DDP achieved similar results (Fig. 5B). Colony formation assays were performed to detect the inhibitory effect of narirutin on the proliferation of single cell. The inhibitory effects of DDP and narirutin on LA795 cell colony formation also showed significant additive effects. The number of colonies was significantly reduced following TMEM16A shRNA knockdown. On this basis, the addition of 30 μM narirutin did not improve the inhibitory effect, whereas the addition of DDP further reduced the number of colonies (Fig. 5C and D). In addition, the above experiments were performed on lung fibroblast 2BS cells, which do not express endogenous TMEM16A. The results showed that narirutin did not inhibit 2BS cell viability (Fig. 5E) or colony number (Fig. 5F and G); however, the inhibitory effect of DDP was broad-spectrum. Therefore, we propose that narirutin inhibits cancer cell proliferation by targeting TMEM16A and enhancing the tumor suppressive effect of DDP.

### 3.6. Narirutin inhibits lung adenocarcinoma cell migration by targeting TMEM16A

The inhibitory effect of narirutin on LA795 cell migration was evaluated using wound healing assays. The results in Fig. 6A showed that narirutin significantly inhibited LA795 cell migration. The statistical results indicated that different concentrations of narirutin inhibited LA795 cell migration in a concentration- and time-dependent manner (Fig. 6B). Additionally, the migration rate of LA795 cells was significantly reduced after shRNA transfection. On this basis, adding 30 μM narirutin did not further inhibit cell migration, which proved that TMEM16A was the target of narirutin in inhibiting LA795 cell migration (Fig. 6C). However, statistical results showed that DDP did not inhibit LA795 cell migration, nor did it potentiate the effect of narirutin (Fig. 6D). This may result from the direct regulation of DNA replication by DDP. Finally, we performed experiments on 2BS cells that did not express TMEM16A, and the results showed that neither narirutin nor

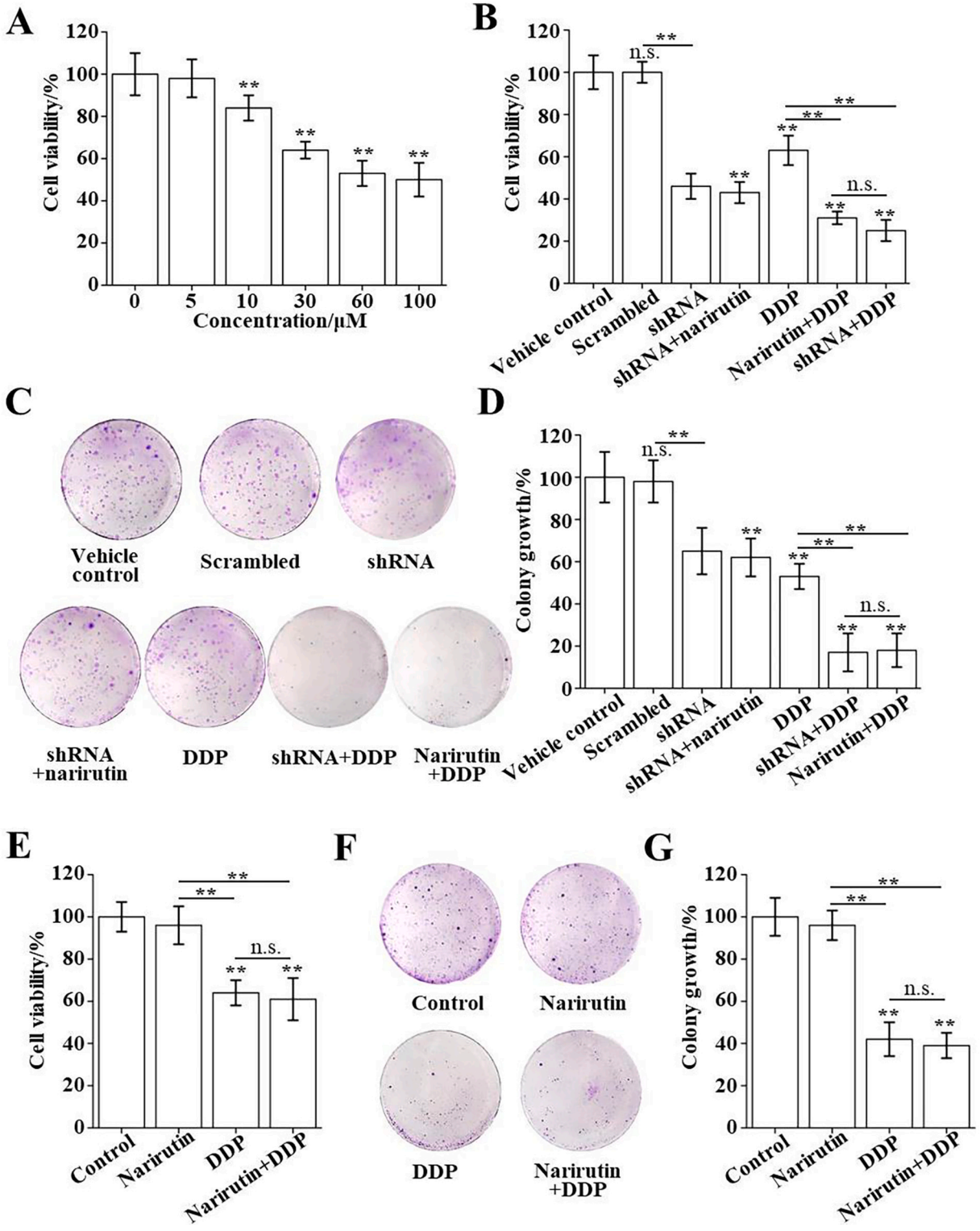


**Fig. 5.** Narirutin inhibited lung cancer cell proliferation targeting TMEM16A. (A). Inhibitory effect of the proliferation of LA795 cells with different concentrations of narirutin ($n = 8$). (B). Inhibitory effect of TMEM16A shRNA, shRNA + 30 μM narirutin, 10 μM DDP, 10 μM DDP + 30 μM narirutin and 10 μM DDP + shRNA to the proliferation and colonies formed of LA795 cells ($n = 8$). (C). Inhibitory effect of TMEM16A shRNA, shRNA + 30 μM narirutin, 10 μM DDP, 10 μM DDP + 30 μM narirutin and 10 μM DDP + shRNA to the colonies formed of LA795 cells ($n = 3$). (D). Statistical results of (C) ($n = 3$). (E). Inhibitory effect of 30 μM narirutin, 10 μM DDP and 10 μM DDP + 30 μM narirutin to the proliferation of 2BS cells ($n = 8$). (F). Inhibitory effect of 30 μM narirutin, 10 μM DDP and 10 μM DDP + 30 μM narirutin to the colonies formed of 2BS cells ($n = 3$). (G). Statistical results of (F) ($n = 3$).

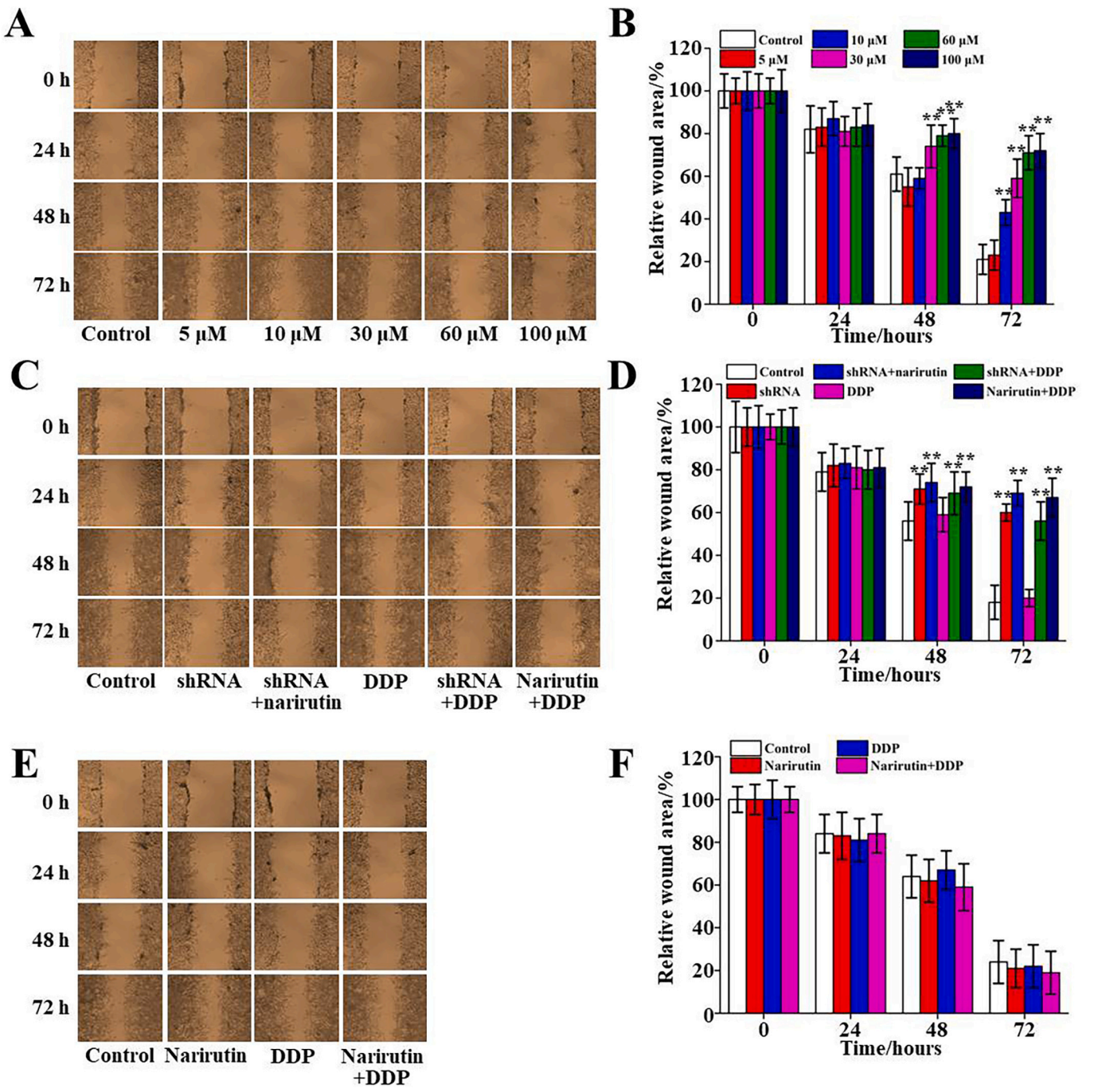


**Fig. 6.** Narirutin inhibited lung cancer cell migration targeting TMEM16A. (A). Inhibitory effect of the migration of LA795 cells with different concentrations of narirutin ($n = 3$). (B). Statistical results of (A) ($n = 3$). (C). Inhibitory effect of TMEM16A shRNA, shRNA + 30 μM narirutin, 10 μM DDP, 10 μM DDP + 30 μM narirutin and 10 μM DDP + shRNA to the migration of LA795 cells ($n = 3$). (D). Statistical results of (C) ($n = 3$). (E). Inhibitory effect of 30 μM narirutin, 10 μM DDP and 10 μM DDP + 30 μM narirutin to the migration of 2BS cells ($n = 3$). (F). Statistical results of (E) ($n = 3$).

DDP affected 2BS cell migration (Fig. 6E and F). The above results indicate that narirutin regulates cancer cell migration by inhibiting TMEM16A, whereas DDP did not affect cancer cell migration.

### 3.7. Narirutin inhibits TMEM16A to enhance DDP induced apoptosis

As high concentrations of DDP strongly induced cancer cell apoptosis, we detected the effect of the combined administration of narirutin and DDP on LA795 apoptosis. LA795 cells incubated with 30, 60, and 120 μM narirutin presented apoptosis rates of 7.27 ± 2.74 %, 22.94 ± 4.88 %, and 54.32 ± 7.21 %, respectively (Fig. 7A–D and G). 10 μM DDP induced a LA795 cell apoptosis rate of 22.14 ± 4.28 % (Fig. 7E), and 10 μM DDP combined with 30 μM narirutin resulted in an apoptosis rate of 56.21 ± 5.21 % (Fig. 7E–F and H). The effect of combined administration of 30 μM narirutin and 10 μM DDP was significantly higher than that of the superposition of the two administrations separately, which indicated that narirutin enhanced the drug sensitivity of LA795 cells to DDP. Based on this result, we speculate that narirutin may delay the resistance to DDP, but further experiments are needed to verify this hypothesis. The apoptosis of 2BS cells that did not express TMEM16A showed that narirutin did not induce apoptosis in 2BS cells (Fig. 7J and K). The combined administration of narirutin and DDP did not promote the apoptosis inducing effects of

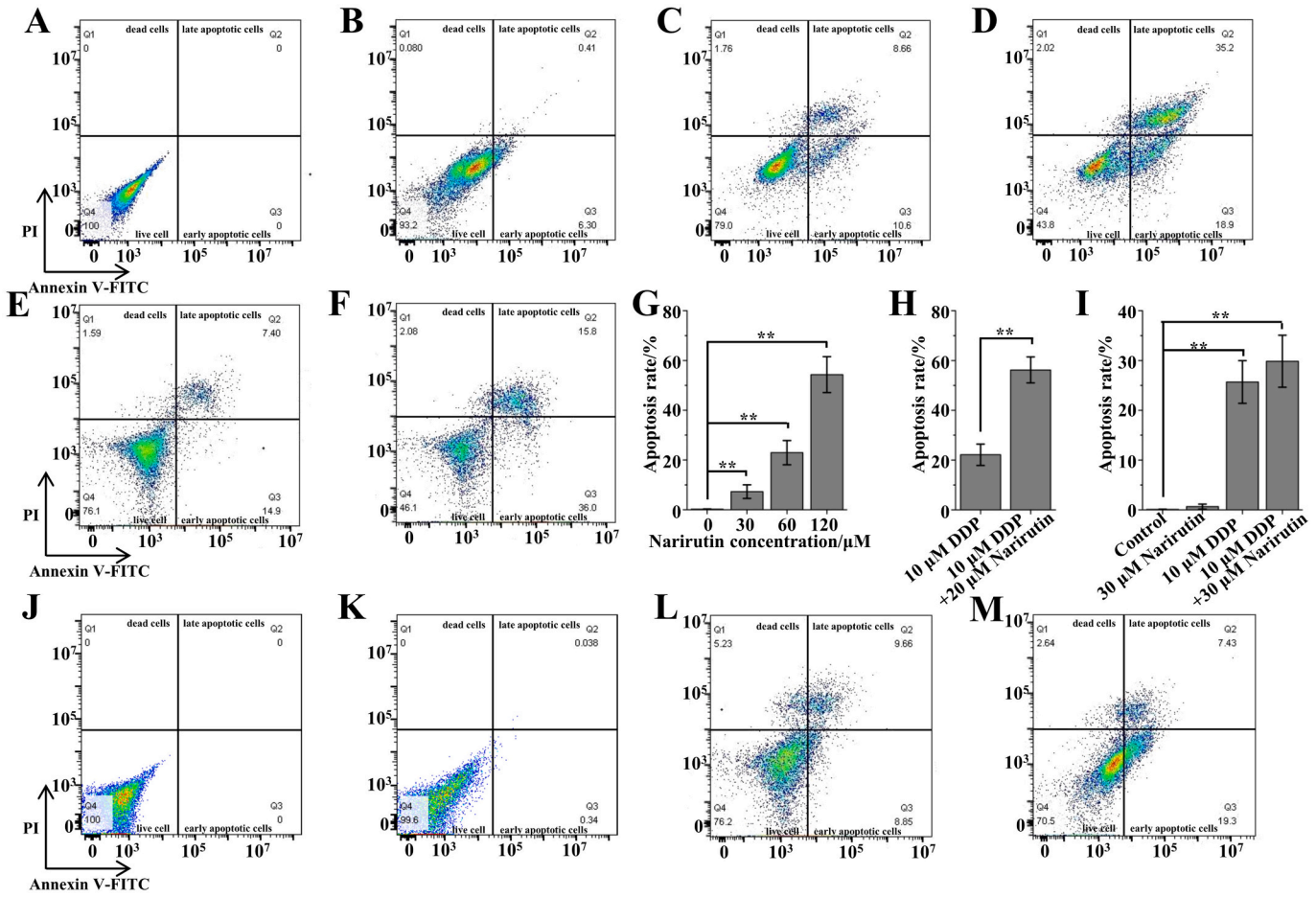


**Fig. 7.** Narirutin promoted lung cancer cell apoptosis targeting TMEM16A. (A–D). LA795 cells apoptosis induced by different concentrations of narirutin ($n = 3$). (E–F). LA795 cells apoptosis induced by 10 μM DDP and 10 μM DDP + 30 μM narirutin ($n = 3$). (G). Statistical results of (A–D) ($n = 3$). (H). Statistical results of (E–F) ($n = 3$). (I). Statistical results of (J–M) ($n = 3$). (J–M). 2BS cells apoptosis induced by 30 μM narirutin, 10 μM DDP and 10 μM DDP + 30 μM narirutin ($n = 3$). Annexin V-FITC (−)/PI (−) for living cells, Annexin V-FITC (+)/PI (−) for early apoptotic cells, Annexin V-FITC (+)/PI (+) for late apoptotic cells, Annexin V-FITC (−)/PI (+) for dead cells.

DDP (Fig. 7L, M, and I). Therefore, we propose that narirutin promotes DDP sensitivity by TMEM16A. These results indicate that low concentrations of narirutin can enhance DDP-induced apoptosis in cells endogenously expressing TMEM16A.

### 3.8. Signal transduction mechanism of narirutin inhibits the growth of LA795 cells

To elucidate the molecular mechanism by which narirutin inhibits the growth of LA795 cells, we detected the expression of proteins related to cell proliferation, migration, and apoptosis. Western blot results showed that incubation of LA795 cells with 30 μM narirutin reduced the phosphorylation of MEK1/2 and ERK1/2 proteins, which affected the expression of downstream cyclin D1 and regulated the cell cycle (Fig. 8A and B). Because narirutin regulated the cell cycle through the MAPK signaling pathway, instead of directly acting on nuclear DNA as DDP, narirutin was less cytotoxic. In addition, narirutin downregulated β-catenin, N-cadherin, and vimentin and upregulated E-cadherin expression (Fig. 8C and D). These proteins were associated with adhesion factors, such as membrane skeleton linkages, and their expression level changes reduced cancer cell motility. Finally, the expression of apoptosis related proteins cleaved-caspase 3 and cleaved-caspase 9 was significantly upregulated by narirutin (Fig. 8E and F). In addition, TMEM16A shRNA also achieved similar regulatory effects (Supplementary Fig. 1). These results indicate that narirutin inhibits TMEM16A, which mediates various signal pathways related to cell proliferation, migration, and apoptosis, resulting in the inhibition of LA795 cell growth.

### 3.9. Narirutin inhibits lung adenocarcinoma growth and potentiates the DDP effect in vivo

*In vitro* experiments showed that the combined administration of narirutin and DDP achieved good anticancer effects, and the side effects and the *in vivo* tumor suppressor effects of the combined administration should be evaluated in tumor xenograft mice. Schematic of the experiments is shown in Fig. 9A. The curve of tumor volume growth with time showed that the tumor volume in the control group continuously increased, whereas the tumor volume of each administration group was inhibited to varying degrees (Fig. 9B). The tumor volume with 30 μM narirutin + 10 μM DDP was lower than that with 60 μM narirutin or 20 μM DDP alone. This result indicated that the combined administration enhanced the sensitivity of drugs *in vivo,* but not only the efficacy of superposition. The growth of mice's body weight over time showed that 20 μM DDP caused weight loss in mice, whereas the other groups gained weight normally (Fig. 9C). Mice were sacrificed, and tumors were dissected after all administrations were completed (Fig. 9D). The results of tumor weight corresponded to those of tumor volume, and the 30 μM narirutin + 10 μM DDP group achieved the highest tumor inhibition rate (Fig. 9E). To further explore the pharmacological mechanism of

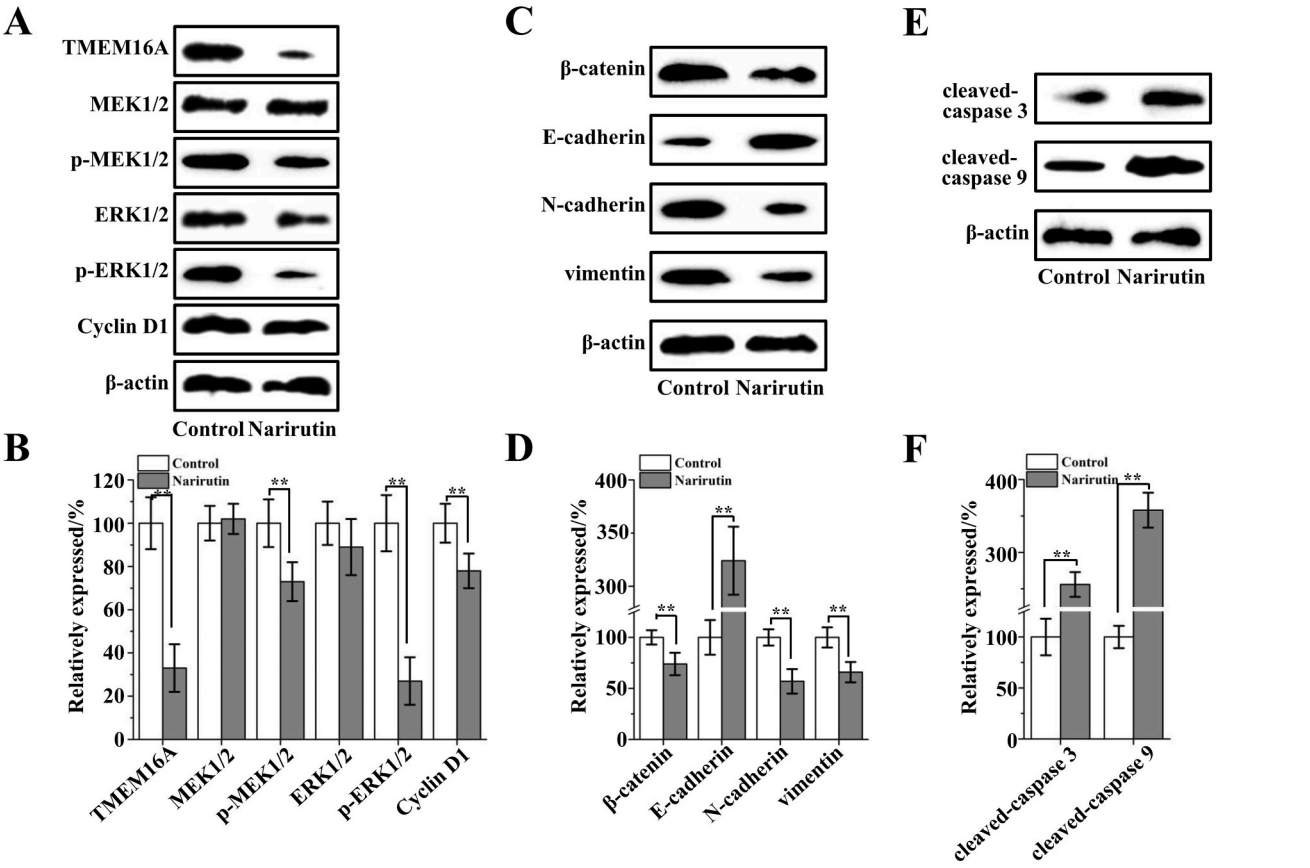


**Fig. 8.** The signal pathway of narirutin inhibited LA795 cell growth. (A). Expression of TMEM16A, MEK1/2, phospho-MEK1/2, ERK1/2, phospho-ERK1/2 and cyclin D1 in 30 μM narirutin incubated LA795 cells ($n = 3$). (B). Statistical results of (A) ($n = 3$). (C). Expression of β-catenin, E-cadherin, N-cadherin, and vimentin in 30 μM narirutin incubated LA795 cells ($n = 3$). (D). Statistical results of (C) ($n = 3$). (E) Expression of cleaved-caspase 3 and cleaved-caspase 9 in 30 μM narirutin incubated LA795 cells ($n = 3$). (F). Statistical results of (E) ($n = 3$).

narirutin *in vivo*, frozen sections and H&E staining were performed on the tumor tissues and organs. The results of pathological sections showed that the livers of mice in the 20 μM DDP group produced multiple round holes and inflammatory infiltration, which might be caused by acute liver injury from high concentrations of DDP (Fig. 9F). Different degrees of cell shrinkage deformation, nuclear lysis was observed in the tumor tissues of all the drug groups, which may be the main reason for tumor inhibition. In conclusion, the narirutin and DDP combined administration group achieved the best anticancer effect without serious side effects.

### 3.10. *In vivo pharmacokinetics of narirutin*

The distribution of narirutin in rats' blood and main organs after intragastric administration was determined by pharmacokinetic experiments. The results showed that the drug concentration in the blood reached a maximum at 1.26 ± 0.30 h, and then the blood concentration gradually decreased. After 24 h, almost no narirutin residue was detected in the blood (Fig. 10A). The pharmacokinetic parameters of narirutin fitted according to blood drug concentration over time were shown in Fig. 10B. The narirutin concentrations in the heart, liver, spleen, lung, kidney, stomach, intestine, and tumor were consistent with those in the blood (Fig. 10C). Narirutin was not detected in the brain, indicating that it could not cross the blood-brain barrier. Everted sac experiments showed that the absorption percentage (Fig. 10D) and cumulative absorption (Fig. 10E) of narirutin increased with time, indicating that the intestinal absorption of narirutin was satisfactory. Therefore, the pharmacokinetic characteristics of narirutin include its rapid metabolism and easy absorption *in vivo*.

## 4. Discussion

This study found that narirutin is a safe and effective functional food for adjuvant therapy of lung adenocarcinoma. Narirutin inhibited endogenous TMEM16A expression and function in lung adenocarcinoma and regulated cancer cell proliferation, migration, and apoptosis. The multi-target combination administration of low concentration narirutin and DDP not only achieved satisfactory therapeutic effects but also eliminated the side effects caused by high concentrations of DDP.

The advantage of narirutin as an adjuvant food treatment for lung adenocarcinoma is its high biosafety. Our study shows that intragastric administration of 60 μM narirutin did not affect the normal weight gain in mice (Fig. 9C). Moreover, pathological sections of mice also show that 60 μM narirutin did not cause damage to the major organs (Fig. 9F). In contrast, the 20 μM DDP group achieved a significant tumor suppressor effect but showed serious toxicity at the same time. The body weight of the 20 μM DDP treated mice continued to decrease with administrations, and the pathological morphology of the liver cells was changed (Fig. 9C and F). The toxicity of DDP results from damage to the membrane structure of normal cells caused by high concentrations of DDP. However, our experiments showed that, unlike DDP, narirutin was safe for normal cells without TMEM16A expression (Fig. 5E, 6F, and 7I). In view of the safety of narirutin and the high efficiency of DDP, low concentration narirutin and DDP co-administration was designed. The targets of narirutin and DDP were different and expected to achieve a mutually reinforcing effect. As expected, the tumor suppression rate of the combined administration of 30 μM narirutin + 10 μM DDP was higher than that of 60 μM narirutin or 20 μM DDP alone, and there were no side effects, such as from 20 μM DDP (Fig. 9). The combined administration

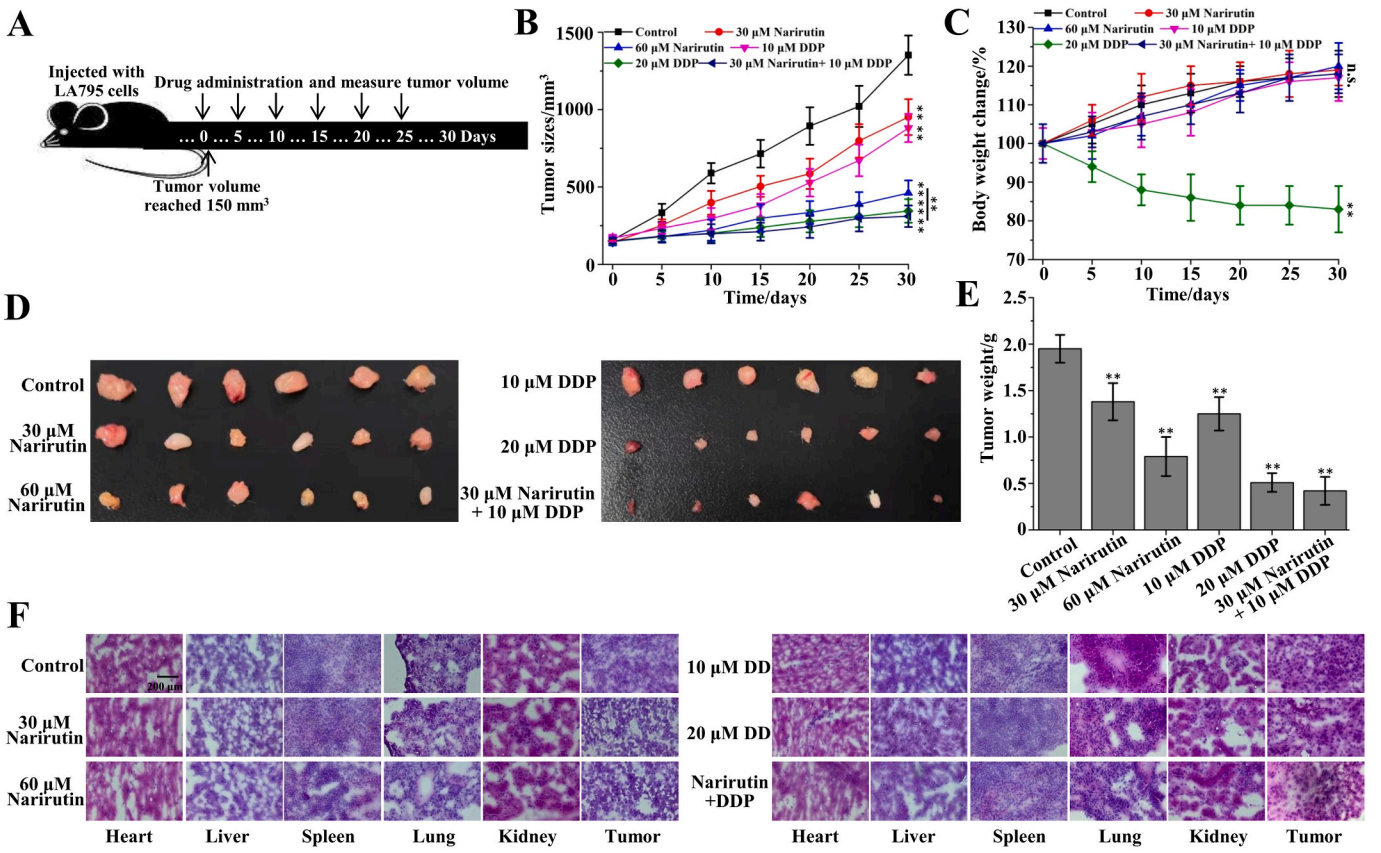


**Fig. 9.** Narirutin inhibited the growth of lung adenocarcinomas *in vivo*. (A). Schematic diagram of the experimental protocol. (B). Tumor volume growth in different groups ($n = 6$). (C). Body weight change curve in different groups ($n = 6$). (D). Images of the tumor tissues after 7 detections ($n = 6$). (E). Statistical results of tumor tissue weight ($n = 6$). (F). Tissue sections of major organ and tumor tissues in different administration groups ($n = 6$).

achieved a dual impact of treating tumors and protecting the body at the same time.

Developing anticancer functional food adjuvant therapy is an important research direction for comprehensive cancer therapy. Various functional foods have been shown to inhibit tumor growth. For example, bamboo fungus polysaccharides can clear superoxide anion free radicals and inhibit lipid peroxidation of cell membranes to anticancer [50]. Curcumin induces non-apoptotic cell death pathways in cancer cells by killing cells resistant to pro-apoptotic stimuli [51]. In addition, the effects of narirutin have been confirmed, including anti-tuberculosis, blood pressure lowering, and anti-allergic (airway inflammation) [52,53]. However, its target and pharmacological mechanisms *in vivo* are unclear. This study confirms that TMEM16A is a key target of narirutin in lung cancer. As TMEM16A is also distributed in vascular smooth muscle and airway tissues, we speculate that the pharmacological action of narirutin in reducing blood pressure and treating allergic airway inflammation may be related to TMEM16A. However, further experimental verification is required. Several studies show that TMEM16A is highly expressed in a variety of cancer cells and closely associated with the growth of cancer cells. TMEM16A regulates multiple functions in lung cancer with rapid growth and easy metastasis. Lung cancer cells H1299 with high expression of TMEM16A grow faster than HBE16 cells with low expression of TMEM16A. The growth of H1299 cells can be inhibited by knocking down or inhibiting TMEM16A [54]. High expression of TMEM16A in human lung adenocarcinoma cell line GLC82 and lung squamous cell line NCI-H520 is positively correlated with cancer cell growth and invasion [55]. TMEM16A is involved in cell proliferation, migration and apoptosis in lung adenocarcinoma LA795 cells [56]. Therefore, TMEM16A can be used as a biomarker and drug target for lung cancer. This study elucidates the molecular mechanism of narirutin's anticancer action as inhibiting TMEM16A to regulate the phosphorylation level of the downstream MAPK signaling pathway. This study clarifies the target and tumor suppressor mechanism of narirutin and provides preliminary data for the development of narirutin as a functional food for anticancer adjuvant therapy.

In addition, the molecular mechanism of narirutin mediated regulation of TMEM16A gating was analyzed by molecular simulation combined with experiments. Although some TMEM16A inhibitors have been identified, the mechanism of their interaction with the TMEM16A protein has not received sufficient attention. The extracellular vestibular region of TMEM16A channels constitutes the inhibitor binding pocket of TMEM16A in both the calcium-bound and -unbound states. The binding sites of various small-molecule inhibitors, such as $CaCC_{inh}$-A01 [49], nuciferine [57], zafirlukast [43], theaflavins [58], and procyanidins [59], are located in this region. In addition, cryo-electron microscopy structural studies showed that the binding sites of 1PBC [60] and niclosamide [61] may be located below the extracellular vestibule or on the side close to TM1. This indicates that the extracellular region of TMEM16A, especially the region above the pore, is a key region for inhibitor binding. We counted the reported binding sites of several inhibitors to TMEM16A (Supplementary Table 1). Residues R515/R535/E624 appeared more frequently, indicating the three residues may possess a broad affinity for the inhibitors. Here, the binding sites of narirutin were identified as R535/E623/E624, which further suggests that R535 and E624 in the extracellular vestibule are key residues for inhibitor binding to TMEM16A. The results provide critical information for rational drug design. Interaction analysis shows that the benzene ring in the structure of narirutin and the hydroxyl group on the sugar ring is key electrostatic interaction sites. This information is important for developing narirutin as an anticancer functional food.

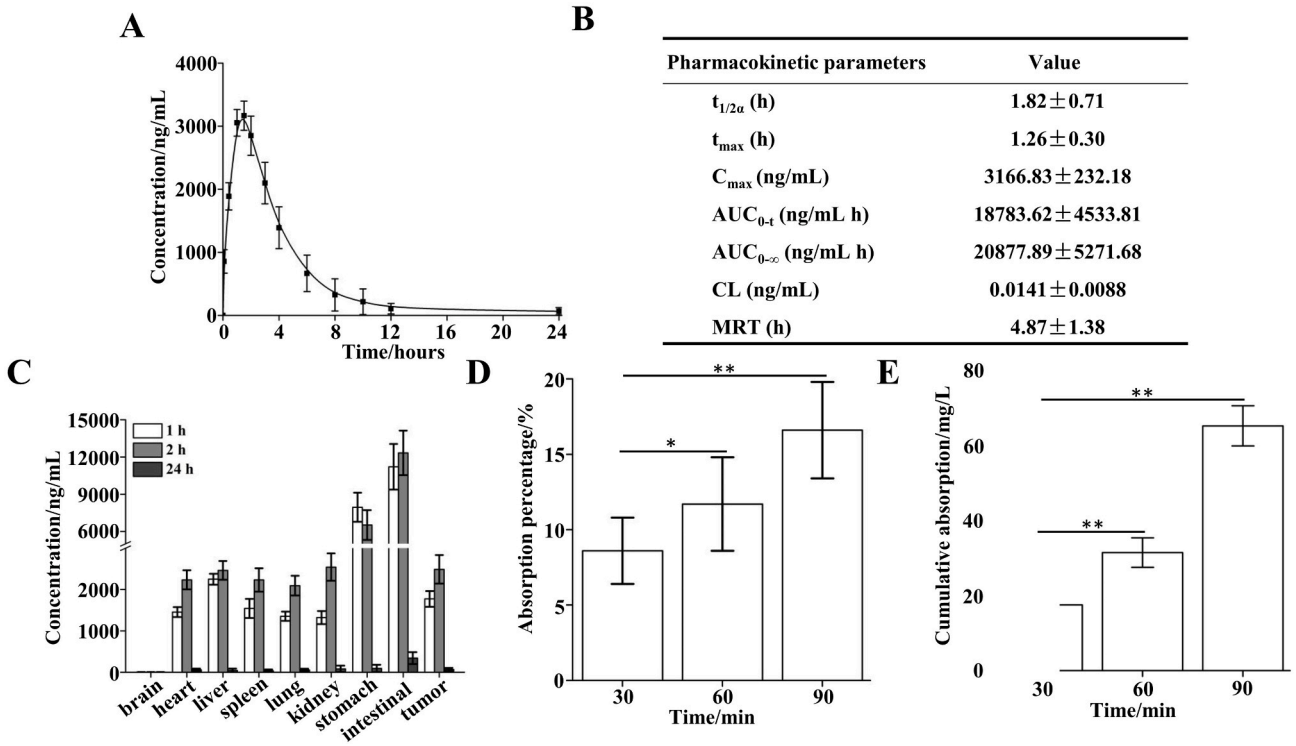


**Fig. 10.** Metabolism and absorption of narirutin in rats. (A). Plasma concentration-time curve of narirutin in rats ($n = 3$). (B). Pharmacokinetics parameters of narirutin intragastric administration ($n = 3$). (C). Major organ distribution of narirutin in rats at 1, 2, and 24 h of intragastric administration ($n = 3$). (D). Absorption percentage of narirutin in rats intestines ($n = 3$). (E). Cumulative absorption of narirutin in rats' intestines ($n = 3$).

Narirutin mainly exists in the peels and seeds of citrus plants of the Rutaceae family, such as grapefruit, tangerines, oranges, and lemons [62]. These plants are major fruits in the tropics and subtropics. They are widely distributed, easy to grow and produce high yields. They have grown in >135 countries worldwide [63]. The narirutin extraction process is simple. The plants are crushed, filtered, concentrated, ethanol-precipitated, and separated using organic solvent. After volatilization, a crude extract is obtained. Narirutin crystals with a purity >95 % can be prepared through multiple crystallizations [64]. Thus, narirutin can be easily used in patients as an adjuvant therapeutic food owing to its low extraction cost and high yield.

In summary, narirutin inhibited the growth of lung cancer cells by targeting TMEM16A. The multi-target combinatorial administration of narirutin and DDP significantly improve the treatment effect on lung cancer and eliminate side effects. Therefore, narirutin may be used as an adjuvant therapeutic functional food along with DDP treatment for lung adenocarcinoma.

## Author statement

This work has not been published previously or under consideration for publication elsewhere.

## CRediT authorship contribution statement

S.G., H.A. and X.K. designed research; S.S., X.B., Q.J., and H.W. performed research and analyzed data; S.G. and S.S. wrote the manuscript; S.G. provided funding for this work.

## Declaration of competing interest

The authors declare that they have no known competing financial interests or personal relationships that could have appeared to influence the work reported in this paper.

## Acknowledgment

This work was supported by the National Natural Science Foundation of China (Grant No. 82104224), Natural Science Foundation of Hebei Province of China (Grant No. C2021201025), Project Funded by China Postdoctoral Science Foundation (Grant No. 2022M710998), Research Project Funded by Postdoctoral of Hebei Province (Grant No. B2022005012), and High-level Talent Research Startup Project of Hebei University (Grant No. 521000981428).

## Appendix A. Supplementary data

Supplementary data to this article can be found online at https://doi.org/10.1016/j.ijbiomac.2022.11.123.

## References

[1] I. Soerjomataram, F. Bray, Planning for tomorrow: global cancer incidence and the role of prevention 2020–2070, Nat. Rev. Clin. Oncol. 18 (10) (2021) 663–672.
[2] R.L. Siegel, K.D. Miller, H.E. Fuchs, A. Jemal, Cancer statistics, 2022, CA Cancer J. Clin. 72 (1) (2022) 7–33.
[3] D. Mukherji, R.H. Murillo, M. Van Hemelrijck, V. Vanderpuye, O. Shamieh, J. Torode, C.S. Pramesh, A. Yusuf, C.M. Booth, A. Aggarwal, R. Sullivan, F. Covid, Cancer task, global cancer research in the post-pandemic world, Lancet Oncol. 22 (12) (2021) 1652–1654.
[4] K.D. Miller, L. Nogueira, T. Devasia, A.B. Mariotto, K.R. Yabroff, A. Jemal, J. Kramer, R.L. Siegel, Cancer treatment and survivorship statistics, 2022, CA Cancer J. Clin. 62 (4) (2022) 220–241.
[5] M.J. Duffy, K. O'Byrne, Tissue and blood biomarkers in lung cancer: a review, Adv. Clin. Chem. 86 (2018) 1–21.
[6] F. Li, L. Yang, Y. Zhao, L. Yuan, S. Wang, Y. Mao, Intraoperative frozen section for identifying the invasion status of lung adenocarcinoma: a systematic review and meta-analysis, Int. J. Surg. 72 (2019) 175–184.
[7] Y. Sakuma, Epithelial-to-mesenchymal transition and its role in EGFR-mutant lung adenocarcinoma and idiopathic pulmonary fibrosis, Pathol. Int. 67 (8) (2017) 379–388.
[8] P.O. Bolan, A. Zviran, L. Brenan, J.S. Schiffman, N. Dusaj, A. Goodale, F. Piccioni, C.M. Johannessen, D.A. Landau, Genotype-fitness maps of EGFR-mutant lung adenocarcinoma chart the evolutionary landscape of resistance for combination therapy optimization, Cell Syst. 10 (1) (2020) 52–65 e7.

[9] S. Liu, R. Wang, Y. Zhang, Y. Li, C. Cheng, Y. Pan, J. Xiang, Y. Zhang, H. Chen, Y. Sun, Precise diagnosis of intraoperative frozen section is an effective method to guide resection strategy for peripheral small-sized lung adenocarcinoma, J. Clin. Oncol. 34 (4) (2016) 307–313.
[10] K.E. Rosenzweig, J.E. Gomez, Concurrent chemotherapy and radiation therapy for inoperable locally advanced non-small-cell lung cancer, J. Clin. Oncol. 35 (1) (2017) 6–10.
[11] S. Seng, Z. Liu, S.K. Chiu, T. Proverbs-Singh, G. Sonpavde, T.K. Choueiri, C.K. Tsao, M. Yu, N.M. Hahn, W.K. Oh, M.D. Galsky, Risk of venous thromboembolism in patients with cancer treated with cisplatin: a systematic review and meta-analysis, J. Clin. Oncol. 30 (35) (2012) 4416–4426.
[12] T.S. Markandeywar, R.K. Narang, D. Singh, V.K. Rai, Targeted delivery of doxorubicin as a potential chemotherapeutic agent, Curr. Drug Deliv. (2022), https://doi.org/10.2174/1567201819666220714101952.
[13] S. Zhao, Y. Tang, R. Wang, M. Najafi, Mechanisms of cancer cell death induction by paclitaxel: an updated review, Apoptosis 27 (9–10) (2022) 647–667.
[14] D. Xie, G. Hu, C. Chen, F. Ahmadinejad, W. Wang, P.L. Li, D.A. Gewirtz, N. Li, Loss of sphingosine kinase 2 protects against cisplatin induced-kidney injury, Am. J. Physiol. Ren. Physiol. 323 (3) (2022) 322–334.
[15] M.Z. Kakabadze, T. Paresishvili, K. Mardaleishvili, Z. Vadachkoria, N. Kipshidze, M. Jangavadze, L. Karalashvili, K. Ghambashidze, D. Chakhunashvili, Z. Kakabadze, Local drug delivery system for the treatment of tongue squamous cell carcinoma in rats, Oncol. Lett. 23 (1) (2022) 13.
[16] T. Kong, L. Chen, X. Zhao, F. Duan, H. Zhou, L. Wang, D. Liu, Anlotinib plus etoposide and cisplatin/carboplatin as first-line therapy for extensive-stage small cell lung cancer (ES-SCLC): a single-arm, phase II study, Investig. New Drugs 40 (5) (2022) 1095–1105.
[17] E.M. Hasan, C.L. Calma, A. Tudor, C. Vernic, E. Palade, E. Tudorache, C. Oancea, I. Papava, Gender differences in coping,depression, and anxiety in patients with non-metastatic lung cancer, Cancer Manag. Res. 14 (2022) 2041–2052.
[18] X.Q. Wang, X.J. Ma, M. Yang, Y. Wang, Y. Xie, W. Hou, Y. Zhang, Proportion and related factors of depression and anxiety for inpatients with lung cancer in China: a hospital-based cross-sectional study, Support Care Cancer 30 (6) (2022) 5539–5549.
[19] Z. Alam, X. Shang, K. Effat, F. Kanwal, X. He, Y. Li, C. Xu, W. Niu, A.R. War, Y. Zhang, The potential role of prebiotics, probiotics, and synbiotics in adjuvant cancer therapy especially colorectal cancer, J. Food Biochem. (2022), e14302, https://doi.org/10.1111/jfbc.14302.
[20] X. Bai, S.T. Li, X.Y. Liu, H.L. An, X.J. Kang, S. Guo, Caffeic acid, an active ingredient in coffee, combines with DOX for multitarget combination therapy of lung cancer, J. Agric. Food Chem. 70 (27) (2022) 8326–8337.
[21] V. Edefonti, G. Randi, C. La Vecchia, M. Ferraroni, A. Decarli, Dietary patterns and breast cancer: a review with focus on methodological issues, Nutr. Rev. 67 (6) (2009) 297–314.
[22] C.B. Ionita-Mindrican, K. Ziani, M. Mititelu, E. Oprea, S.M. Neacsu, E. Morosan, D. E. Dumitrescu, A.C. Rosca, D. Draganescu, C. Negrei, Therapeutic benefits and dietary restrictions of fiber intake: a state of the art review, Nutrients 14 (13) (2022).
[23] X.S. He, K.N. Wu, X.H. Zhang, R. Nishihara, Y. Cao, C.S. Fuchs, E.L. Giovannucci, S. Ogino, A.T. Chan, M.Y. Song, Dietary intake of fiber, whole grains and risk of colorectal cancer: an updated analysis according to food sources, tumor location and molecular subtypes in two large US cohorts, Int. J. Cancer 145 (11) (2019) 3040–3051.
[24] A. Dandamudi, J. Tommie, L. Nommsen-Rivers, S. Couch, Dietary patterns and breast cancer risk: a systematic review, Anticancer Res. 38 (6) (2018) 3209–3222.
[25] S.W. Tay, J.W. Li, K.M. Fock, Diet and cancer of the esophagus and stomach, Curr. Opin. Gastroenterol. 37 (2) (2021) 158–163.
[26] L.L. Cui, F. Xu, K. Wu, L. Li, T.Y. Qiao, Z.L. Li, T.T. Chen, C.Q. Sun, Anticancer effects and possible mechanisms of lycopene intervention on N-methylbenzylnitrosamine induced esophageal cancer in F344 rats based on PPAR gamma(1), Eur. J. Pharmacol. 881 (2020).
[27] S. Tanasawet, W. Sukketsiri, P. Chonpathompikunlert, W. Klaypradit, M. Sroyraya, P. Hutamekalin, Apoptotic effect of astaxanthin from white shrimp shells on lung cancer A549 cells, Trop. J. Pharm. Res. 19 (9) (2020) 1835–1842.
[28] S. Saffarionpour, L.L. Diosady, Delivery of curcumin through colloidal systems and its applications in functional foods, Curr. Opin. Food Sci. 43 (2022) 155–162.
[29] P.B. Bhosale, S.E. Ha, P. Vetrivel, H.H. Kim, S.M. Kim, G.S. Kim, Functions of polyphenols and its anticancer properties in biomedical research: a narrative review, Transl. Cancer Res. 9 (12) (2020) 7619–7631.
[30] S. Guo, X. Bai, S. Shi, Y. Deng, X. Kang, H. An, TMEM16A, a homoharringtonine receptor, as a potential endogenic target for lung cancer treatment, Int. J. Mol. Sci. 22 (20) (2021).
[31] S. Guo, X. Bai, Y. Liu, S. Shi, X. Wang, Y. Zhan, X. Kang, Y. Chen, H. An, Inhibition of TMEM16A by natural product silibinin: potential lead compounds for treatment of lung adenocarcinoma, Front. Pharmacol. 12 (2021), 643489.
[32] D. Crottes, L.Y. Jan, The multifaceted role of TMEM16A in cancer, Cell Calcium 82 (2019).
[33] S. Guo, X. Bai, S. Shi, S. Li, X. Liu, H. An, X. Kang, Multi-target tracheloside and doxorubicin combined treatment of lung adenocarcinoma, Biomed. Pharmacother. 153 (2022), 113392.
[34] A. Hao, S. Guo, S. Shi, X. Wang, Y. Zhan, Y. Chen, H. An, Emerging modulators of TMEM16A and their therapeutic potential, J. Membr. Biol. 254 (4) (2021) 353–365.
[35] S. Guo, Y. Chen, S. Shi, X. Wang, H. Zhang, Y. Zhan, H. An, Arctigenin, a novel TMEM16A inhibitor for lung adenocarcinoma therapy, Pharmacol. Res. 155 (2020), 104721.
[36] S. Guo, L. Qiu, Y. Chen, X. Wang, B. Ma, C. Qu, J. Cui, H. Zhang, C. Xing, Y. Zhan, H. An, TMEM16A-inhibitor loaded pH-responsive nanoparticles: a novel dual-targeting antitumor therapy for lung adenocarcinoma, Biochem. Pharmacol. 178 (2020), 114062.
[37] O. Trott, A.J. Olson, Software news and update AutoDock Vina: improving the speed and accuracy of docking with a new scoring function,efficient optimization, and multithreading, J. Comput. Chem. 31 (2) (2010) 455–461.
[38] G.M. Morris, R. Huey, W. Lindstrom, M.F. Sanner, R.K. Belew, D.S. Goodsell, A. J. Olson, AutoDock4 and AutoDockTools4: automated docking with selective receptor flexibility, J. Comput. Chem. 30 (16) (2009) 2785–2791.
[39] W. Namkung, R.D. Carpenter, A.S. Verkman, Small-molecule activators and inhibitors of calcium-activated chloride channel, Tmem16a, Pediatr. Pulm. (2009) 288.
[40] W. Namkung, P.W. Phuan, A.S. Verkman, TMEM16A inhibitors reveal TMEM16A as a minor component of calcium-activated chloride channel conductance in airway and intestinal epithelial cells, J. Biol. Chem. 286 (3) (2011) 2365–2374.
[41] S. Guo, Y. Chen, C. Pang, X. Wang, S. Shi, H. Zhang, H. An, Y. Zhan, Matrine is a novel inhibitor of the TMEM16A chloride channel with antilung adenocarcinoma effects, J. Cell. Physiol. 234 (6) (2019) 8698–8708.
[42] B.R. Brooks, C.L. Brooks, A.D. Mackerell, L. Nilsson, R.J. Petrella, B. Roux, Y. Won, G. Archontis, C. Bartels, S. Boresch, A. Caflisch, L. Caves, Q. Cui, A.R. Dinner, M. Feig, S. Fischer, J. Gao, M. Hodoscek, W. Im, K. Kuczera, T. Lazaridis, J. Ma, V. Ovchinnikov, E. Paci, R.W. Pastor, C.B. Post, J.Z. Pu, M. Schaefer, B. Tidor, R. M. Venable, H.L. Woodcock, X. Wu, W. Yang, D.M. York, M. Karplus, CHARMM: the biomolecular simulation program, J. Comput. Chem. 30 (10) (2009) 1545–1614.
[43] S. Shi, B. Ma, F.D. Sun, C. Qu, G. Li, D.H. Shi, W.X. Liu, H.L. Zhang, H.L. An, Zafirlukast inhibits the growth of lung adenocarcinoma via inhibiting TMEM16A channel activity, J. Biol. Chem. 298 (3) (2022).
[44] P.F. Li, K.M. Merz, Taking into account the ion-induced dipole interaction in the nonbonded model of ions, J. Chem. Theory Comput. 10 (1) (2014) 289–297.
[45] P.F. Li, B.P. Roberts, D.K. Chakravorty, K.M. Merz, Rational design of particle mesh Ewald compatible Lennard-Jones parameters for +2 metal cations in explicit solvent, J. Chem. Theory Comput. 9 (6) (2013) 2733–2748.
[46] W. Humphrey, A. Dalke, K. Schulten, VMD: visual molecular dynamics, J. Mol. Graph. 14 (1) (1996) 33–38, 27-8.
[47] M. Frisch, G.W. Trucks, H. Schlegel, G. Scuseria, M. Robb, J. Cheeseman, J. Montgomery, T. Vreven, K. Kudin, J. Burant, Gaussian 03, 2004.
[48] T. Lu, F.W. Chen, Multiwfn: a multifunctional wavefunction analyzer, J. Comput. Chem. 33 (5) (2012) 580–592.
[49] S. Shi, S.A. Guo, Y.F. Chen, F. Sun, C.L. Pang, B.A. Ma, C. Qu, H.L. An, Molecular mechanism of CaCCinh-A01 inhibiting TMEM16A channel, Arch. Biochem. Biophys. 695 (2020).
[50] K.Y. Park, X. Zhao, S.H. Mun, Anticancer effects of bamboo salt on human cancer cells and on buccal mucosa cancer in mice, FASEB J. 27 (2013).
[51] F. Lefranc, N. Tabanca, R. Kiss, Assessing the anticancer effects associated with food products and/or nutraceuticals using in vitro and in vivo preclinical development-related pharmacological tests, Semin. Cancer Biol. 46 (2017) 14–32.
[52] P.K. Sahu, P.K. Mohapatra, D.P. Rajani, M.K. Raval, Structure-based discovery of narirutin as a shikimate kinase inhibitor with anti-tubercular potency, Curr. Comput.-Aid Drug 16 (5) (2020) 523–529.
[53] N. Funaguchi, Y. Ohno, B.L.B. La, T. Asai, H. Yuhgetsu, M. Sawada, G. Takemura, S. Minatoguchi, T. Fujiwara, H. Fujiwara, Narirutin inhibits airway inflammation in an allergic mouse model, Clin. Exp. Pharmacol. Physiol. 34 (8) (2007) 766–770.
[54] C. Hu, R.G. Zhang, D.P. Jiang, TMEM16A as a potential biomarker in the diagnosis and prognosis of lung cancer, Arch. Iran. Med. 22 (1) (2019) 32–38.
[55] L.H. Jia, W. Liu, L.Z. Guan, M. Lu, K.W. Wang, Inhibition of calcium-activated chloride channel ANO1/TMEM16A suppresses tumor growth and invasion in human lung cancer, Plos One 10 (8) (2015).
[56] X. Zhang, G.H. Zhang, W.J. Zhai, Z.J. Zhao, S. Wang, J.F. Yi, Inhibition of TMEM16A Ca2+-activated Cl- channels by avermectins is essential for their anticancer effects, Pharmacol. Res. 156 (2020).
[57] X. Bai, X. Liu, S. Li, H. An, X. Kang, S. Guo, Nuciferine inhibits TMEM16A in dietary adjuvant therapy for lung cancer, J. Agric. Food Chem. 70 (12) (2022) 3687–3696.
[58] S. Shi, B. Ma, F. Sun, C. Qu, H. An, Theaflavin binds to a druggable pocket of TMEM16A channel and inhibits lung adenocarcinoma cell viability, J. Biol. Chem. 297 (3) (2021), 101016.
[59] C. Li, S. Shi, D. Gao, B. Li, G. Song, Y. Chen, H. An, C. Xing, Near-infrared light-responsive nanoinhibitors for tumor suppression through targeting and regulating anion channels, ACS Appl. Mater. Interfaces 14 (28) (2022) 31715–31726.
[60] A.K.M. Lam, S. Rutz, R. Dutzler, Inhibition mechanism of the chloride channel TMEM16A by the pore blocker 1PBC, Nat. Commun. 13 (1) (2022).
[61] Y. Cheng, S. Feng, C. Puchades, J. Ko, E. Figueroa, Y. Chen, H. Wu, S. Gu, T. Han, J. Li, B. Ho, B. Shoichet, Y.N. Jan, L. Jan, Identification of a conserved drug binding pocket in TMEM16 proteins, Res. Square (2022), https://doi.org/10.21203/rs.3.rs-1296933/v1.
[62] G. Raman, G.K. Jayaprakasha, J. Brodbelt, M.H. Cho, B.S. Patil, Isolation of structurally similar citrus flavonoids by flash chromatography, Anal. Lett. 37 (14) (2004) 3005–3016.
[63] J.C.S. Carvalho, J.R. Pirani, M.J.P. Ferreira, Esenbeckia (Pilocarpinae, Rutaceae): chemical constituents and biological activities, Braz. J. Bot. 45 (1) (2022) 41–65.
[64] S. Lee, C.S. Khoo, J.L. Pearson, J.R. Hennell, A. Bensoussan, Liquid chromatographic determination of narirutin and hesperidin in Zhi Ke (Citrus aurantium L.) in the form of the raw herb and of the dried aqueous extract, J. AOAC Int. 92 (3) (2009) 789–796.